Journal of
Materials Chemistry A

ROYAL SOCIETY
OF CHEMISTRY

PAPER

View Article Online
View Journal | View Issue

Cite this: *J. Mater. Chem. A*, 2021, **9**, 11651

Freestanding interlayers for Li–S batteries: design and synthesis of hierarchically porous N-doped C nanofibers comprising vanadium nitride quantum dots and MOF-derived hollow N-doped C nanocages†

Rakesh Saroha,[a] Jang Hyeok Oh,[a] Young Hoe Seon,[a] Yun Chan Kang,[b] Jae Seob Lee,[a] Do Won Jeong[a] and Jung Sang Cho *[a]

Received 2nd March 2021
Accepted 16th April 2021

DOI: 10.1039/d1ta01802g

rsc.li/materials-a

The introduction of a functional interlayer between the cathode and anode in lithium–sulfur battery (LSB) technology results in significant improvements in electrochemical performance. Here, we developed hierarchically structured porous, conductive, and multifunctional N-doped carbon (N-C) nanofibers comprising homogeneously dispersed vanadium nitride quantum dots and hollow N-C nanocages as functional interlayers for advanced LSBs. The freestanding interlayer contains well-developed long-range channels and numerous interconnected hollow N-C nanocages derived from the metal–organic framework. Furthermore, the presence of a N-C framework and vanadium nitride quantum dots measuring several nanometers improves the redox reaction kinetics and provides numerous chemisorption sites for the effective trapping and reuse of lithium polysulfide. As a result, the assembled Li–S cell employing the unique nanostructured freestanding interlayer exhibits superior rate capability and stable cycling performance (decay rate of 0.02% per cycle at 0.5C) considering the high sulfur content (80 wt%) and loading (*ca.* 4 mg cm^{-2}) in the sulfur electrodes. Even with an ultra-high sulfur loading of 11.0 mg cm^{-2}, the Li–S cell delivered a stable areal capacity of 5.0 mA h cm^{-2} after 100 charge–discharge cycles at 0.05C. Thus, the uniquely nanostructured interlayer shows high potential for the development of advanced LSBs utilizing pure sulfur electrodes with realistic battery parameters.

Introduction

Among the currently available energy storage systems, lithium-ion battery (LIB) technology has achieved great success, particularly in portable electronic devices and large-scale energy storage systems, such as electric vehicles, owing to their high gravimetric and volumetric energy densities.[1–9] However, because LIBs are approaching their theoretical capacities, there is a worldwide push for the development of other energy storage systems with higher energy/volume densities made from abundant resources and having low processing costs. In this regard, lithium–sulfur batteries (LSBs) have tremendous potential as next-generation energy storage systems owing to their high theoretical specific discharge capacity (1675 mA h g^{-1}), high energy density (2600 W h kg^{-1}), moderate average operating voltage (approximately 2.2 V *vs.* Li$^+$/Li), and low processing costs due to the use of earth-abundant sulfur.[10–14] Nevertheless, the practical utilization of LSBs is currently restrained by several fundamental problems, including (1) the highly insulating nature of elemental sulfur ($\sigma \approx 10^{-30}$ S cm^{-1} at ambient temperature) and its discharge product, *i.e.*, Li_2S ($\sigma \approx 10^{-13}$ S cm^{-1}), which results in reduced active material utilization after repeated cycling, (2) the formation and migration of lithium polysulfides (LiPSs) toward the anode during discharge, which results in the well-known "shuttle effect" and subsequently leads to capacity fading because of the continuous loss of the active material, and (3) the severe volume changes during conversion between S and Li_2S arising from the density difference (2.03 and 1.66 g cm^{-3} for S and Li_2S, respectively) that leads to electrode pulverization.[15–21] These problems cause cascade effects that result in substandard electrochemical performance, inferior cyclability, poor rate performance, and low coulombic efficiencies. Tremendous efforts to resolve these issues have been made during the last decade, for example, the use of nanocomposites as advanced sulfur hosts with porous conductive matrices, such as carbon

---

[a] *Department of Engineering Chemistry, Chungbuk National University, Chungbuk 361-763, Republic of Korea. E-mail: jscho@cbnu.ac.kr; Fax: +82-43-262-2380; Tel: +82-43-261-2489*

[b] *Department of Materials Science and Engineering, Korea University, 145, Anam-Ro, Seongbuk-Gu, Seoul 02841, Republic of Korea*

† Electronic supplementary information (ESI) available. See DOI: 10.1039/d1ta01802g

nanotubes (CNTs),[22,23] activated carbon,[24] graphene,[25] and reduced graphene oxide,[26,27] for the physical confinement of LiPSs. Many other strategies based on the chemical anchoring of LiPSs using, for example, metal compounds,[28–31] electrolyte additives/modification,[32,33] and doping/coating,[34,35] have been reported so far.

Recently, an effective strategy to improve the electrochemical performance of LSBs that is gaining momentum is the incorporation of modified cell components as a porous interlayer between the cathode and anode.[36–41] This so-called functional interlayer generally consists of a thin coating of porous carbonaceous materials, polymers, and metal oxides deposited on the cathode-facing side of the separator or as a freestanding interlayer that acts as a barrier to LiPS migration to the anode, *i.e.*, lithium.[42–44] The interlayer performs three main functions, namely, (1) blocking the migration of LiPSs to the anode side and, thus, preventing the loss of active materials, (2) enabling the reuse of entrapped/dissolved LiPSs to guarantee high sulfur consumption during repeated cycling, and (3) reducing the severe volume variation of the active material during lithiation/delithiation. However, to be suitable for use as an interlayer, the material should possess high porosity, high electrical conductivity, and abundant surface chemisorption capability to enable polysulfide confinement.

Thus, in this study, we adopted three concepts/components: a hierarchically porous structure, polar metal nitride quantum dots, and a highly conductive C matrix composed of hollow N-doped carbon (N-C) nanocages, and we used the electrospinning process as a novel way to obtain a multifunctional interlayer for LSBs. To achieve a porous structure, both zeolitic imidazolate frameworks (ZIF-8) and polystyrene (PS) were used in combination as hierarchically structured pore generators. ZIF-8, a class of metal–organic frameworks (MOFs), is composed of tetrahedrally coordinated Zn ions connected through organic linkers (imidazolate) and has a high surface area, tunable pore size, and easy structural design.[45–48] Likewise, as a pore modulator, PS forms homogenous tunnel-like continuous longitudinal channels throughout the interlayer. The unique hierarchically porous nanostructure results in efficient electrolyte percolation, which enhances Li-ion diffusion and reaction kinetics. In addition, the volume change or strain developed during the conversion reaction between S and Li_2S can also be mitigated; hence, pulverization of the electrode can be inhibited, especially when using electrodes having ultra-high sulfur loading. Polar metal nitride quantum dots (vanadium nitride, VN, in this study) were embedded in the N-C matrix to anchor lithium polysulfides and prevent their migration towards the anode. VN has a high electron conductivity of approximately 10^4 S cm^{-1}, which results in the rapid electron transfer needed for polysulfide oxidation back to elemental sulfur and provides a catalytic effect to improve polysulfide trapping and conversion.[49–51] Thus, the N-doped C nanofiber (N-CNF) matrix acts as a highly conductive scaffold to provide large channels for Li-ion transport and electron conduction to achieve enhanced reaction kinetics. Moreover, porous N-CNFs could also increase the physical adsorption of polar polysulfides, although to a lesser extent, owing to their non-polar nature. This formation of hierarchically porous and highly conductive VN quantum dot-embedded C nanofibers was achieved by electrospinning followed by facile heat-treatment, thus yielding a multifunctional freestanding interlayer.

In general, ultra-high-loading sulfur electrodes are composed of freestanding films, and, thus, no current-collector is employed (that is, they are aluminum-free) during the electrochemical reaction. However, such an aluminum-free arrangement is highly undesirable from the point of view of commercialization because of the high operating costs. Therefore, we utilized hierarchically porous N-C nanofibers comprising VN quantum dots and hollow N-C nanocages (N-CNF@VN/HNC) as a freestanding, multifunctional interlayer between the lithium anode and pure sulfur cathode. The unique hybrid interlayer was used in advanced LSBs with realistic battery parameters, specifically, a pure sulfur electrode with a high sulfur content (80 wt% of elemental sulfur), ultra-high sulfur loading (*ca.* 4, 8.2, and 11 mg cm^{-2}), and extremely low electrolyte/sulfur ratio (*ca.* 8 μL mg^{-1}). The low-cost and facile synthesis yielded the unique N-CNF@VN/HNC structure, which is a promising multifunctional interlayer for advanced LSBs and could open new avenues of investigation for practical metal–sulfur battery technology.

Experimental

Chemicals

Nanofibers were prepared using analytical grade chemicals: PS (M_w = 192 000, Sigma-Aldrich), polyacrylonitrile (PAN, M_w = 150 000, Sigma-Aldrich), vanadium pentoxide (V_2O_5, 99.0%, Daejung Chemicals), urea (NH_2CONH_2, 99.0%, Samchun Chemicals), 2-methylimidazole (M_w = 82.10, 99%, Acros Organics), and $Zn(NO_3)_2 \cdot 6H_2O$ (96.0%, Junsei). All chemicals were used as received. The solvent used for the spinning solution was *N*,*N*-dimethylformamide (DMF, 99.5%, Samchun Chemicals).

Preparation of interlayer structures

N-CNF@VN/HNC was prepared by electrospinning and subsequent simple heat treatment. First, an as-spun V_2O_5/ZIF-8/PAN/PS composite fiber web was prepared by electrospinning. For this, ZIF-8 polyhedra were synthesized. Briefly, 0.732 g of $Zn(NO_3)_2 \cdot 6H_2O$ was added to 30 mL of methanol with continuous stirring. A separate solution of 2-methylimidazole (1.6 g) in methanol (40 mL) was added dropwise to the above solution, which was stirred for 6 h. Finally, the obtained suspension was centrifuged, washed, and dried in an oven at 80 °C to obtain ZIF-8 polyhedra. The spinning solution was prepared by adding 10.0 g of PS to 70 mL of DMF at 40 °C with continuous stirring. Subsequently, 2.0 g of the prepared ZIF-8 polyhedra and 5.0 g PAN were added to the above solution, followed by addition of V_2O_5 powder (0.5 g), and the solution was stirred overnight to achieve homogenous mixing. Finally, the obtained yellowish gel-like V_2O_5/ZIF-8/PAN/PS DMF solution was loaded into a 12 mL hypodermic syringe pump fitted with a stainless-steel needle (21 gauge). A voltage of 25 kV was applied between the collector (Al foil) and the needle. The distance between the Al foil collector and tip of the needle was fixed at 15 cm. The solution was then fed through the needle at a flow rate of 4 mL h^{-1}. In addition, the temperature and relative humidity were approximately 24 °C and 30%, respectively. N-CNF@VN/HNC was finally obtained by heat treatment of the as-spun V_2O_5/ZIF-8/PAN/PS composite fibers at 800 °C for 5 h in a N_2 atmosphere in the presence of urea. Likewise, as-spun ZIF-8/PAN/PS composite fibers without V_2O_5 were also prepared *via* electrospinning and heat treatment at 800 °C for 5 h in a N_2 atmosphere in the presence of urea for the preparation of hierarchically porous N-C nanofibers with hollow N-C nanocages (N-CNF@HNC) that do not contain VN quantum dots. For a better comparison, composite fibers of PAN/PS only without V_2O_5 and ZIF-8 were prepared by electrospinning and heat treated at 800 °C for 5 h in a N_2 atmosphere in the presence of urea, yielding porous N-C nanofibers as a standard for comparison. These are abbreviated as N-CNFs.

Physical characterization

The crystal structures and phases of the synthesized nanofibers were determined using a X-ray diffractometer (XRD), D8 Discover, with a general area detector diffraction system (GADDS), Bruker). A Cu $K_{\alpha1}$ radiation source (1.5405 Å) was used and measurements were carried out in the 2θ range of 10–70° with a step size of 0.02°. The microstructure was observed by field-emission scanning electron microscopy (FE-SEM, ULTRA PLUS, ZEISS, operated at 15 kV) and field-emission transmission electron microscopy (FE-TEM, JEOL, JEM-2100F-200 kV). The Brunauer–Emmett–Teller (BET) isotherm was used to determine the specific surface area and pore volume from N_2 adsorption–desorption isotherms using a porosity and surface area analyzer. The optimized heating temperature for the as-spun nanofibers and quantification of the carbon content after heat treatment was determined by thermogravimetric analysis (TGA, Pyris 1, PerkinElmer). All the samples were heated to 800 °C from room temperature at a heating rate of 5 °C min^{-1} unless mentioned otherwise. UV-visible spectroscopy was used for polysulfide absorption tests using a UV-vis spectrometer (Lambda 35, PerkinElmer) from 200 to 800 nm. Raman spectroscopy (LabRam, HR800, Horiba Jobin-Yvon) was performed to characterize the crystalline nature of the carbonaceous material in the prepared samples. X-ray photoelectron spectroscopy (XPS) measurements were carried out to analyze the chemical states of all elements using a Thermo Scientific K-Alpha spectrometer with a monochromatic Al K_α X-ray source. The energy step size was 0.10 eV.

Sulfur cathode preparation and cell assembly

Regular sulfur cathodes were prepared as working electrodes for electrochemical analyses using a slurry casting method. Briefly, elemental sulfur, carbon black (Super-P), and polyvinylidene fluoride (PVDF) binder were mixed in a weight ratio of 8 : 1 : 1 and dispersed in a minimum amount of *N*-methyl-2-pyrrolidone (NMP) solvent. The slurry was stirred overnight to yield a homogeneous mixture and then coated onto the aluminum-foil current collector, followed by heating at 60 °C overnight to evaporate the solvent completely. The working electrodes were punched into circular disks (∅ = 14 mm) having an average sulfur loading of *ca.* 4 mg cm^{-2} and subsequently transferred to an argon-filled glove box (H_2O and O_2 < 0.5 ppm) after drying at 50 °C for 30 min. CR2032 coin-cells were assembled using the working electrode as the cathode, lithium metal (∅ = 14 mm) as the anode, and polypropylene (∅ = 20 mm, Celgard) as the separator. For the interlayer cell arrangement, circular disks of N-CNF@VN/HNC, N-CNF@HNC, and N-CNF (∅ = 14 mm, loading approximately 2.6 mg cm^{-2}) were used. The electrolyte was 1.0 mol L^{-1} lithium bis(trifluoromethanesulfonyl)imide (LiTFSI) in a mixture of 1,3-dioxolane (DOL) and 1,2-dimethoxyethane (DME) (1 : 1, by volume) with 0.5 mol L^{-1} $LiNO_3$ additive. The total amount of electrolyte used inside the cells was limited to approximately 8 μL mg^{-1}.

Electrochemical measurements

Electrochemical impedance spectra (EIS) of the Li–S cells were obtained in the frequency range of 2 MHz to 0.01 Hz using an impedance analyzer (ZIVESP2 Electrochemical Workstation). The amplitude of the alternating current (AC) pulse was fixed at 5 mV. Cyclic voltammetry (CV) tests were performed at different scan rates ranging from 0.05–0.3 mV s^{-1}, and charge–discharge tests were conducted at various rates (0.05–2.0C) using a WBCS3000 battery cycler (WonATech). The voltage range for CV and cycling tests was fixed at 1.5–2.8 V throughout the measurements. The C-rate was calculated by equating 1.0C to 1675 mA h g^{-1}. Prolonged cycling performance was also determined at C-rates of 0.1, 0.5, 1.0, and 1.5. In addition, cells with ultra-high sulfur loadings (8.2, and 11.0 mg cm^{-2}) were assembled, and their cycling performance was observed at 0.05C.

Polysulfide adsorption study

To achieve the visual demonstration of polysulfide adsorption, experiments were conducted using a lithium polysulfide solution. Sulfur powder and lithium sulfide (Li_2S, ≥ 99%, Sigma-Aldrich) in a 1 : 5 mixture were added to an appropriate amount of DOL : DME (1 : 1, v/v) to yield 2.0 M sulfur in the form of Li_2S_6. Glass vials containing the sample were filled with lithium polysulfide solution (1.0 mM of Li_2S_6 in an appropriate amount of DOL : DME (1 : 1)) and stirred inside a glove box. A blank polysulfide solution was also prepared as a standard.

Symmetric cell assembly for electrocatalytic activity test

Symmetric cells were assembled using different interlayer arrangements to study the electrocatalytic activity towards lithium polysulfides. The synthesized interlayer materials were mixed with carbon black and PVDF binder in a weight ratio of 8 : 1 : 1 with NMP as the solvent. The homogeneous slurry was coated on aluminum foil and dried at 60 °C overnight. Circular electrodes of ∅ = 14 mm were cut. The symmetric cells were assembled using N-CNF@VN/HNC or N-CNF@HNC or N-CNF electrodes as the counter and working electrodes separated by a Celgard 2400 membrane. The electrolyte used was 40 μL of

0.25 M Li_2S_6 solution prepared in DOL/DME solvent containing 1.0 mol L^{-1} LiTFSI salt. CV tests for symmetric cells were performed at a scan rate of 3 mV s^{-1} in a voltage window of −1.5 to 1.5 V. A symmetric cell comprising N-CNF@VN/HNC as the electrode and without Li_2S_6 solution was also assembled for comparison.

Results and discussion

Hierarchically porous N-C nanofibers comprising VN quantum dots and hollow N-C nanocages were prepared by electrospinning followed by simple heat treatment. Scheme 1 shows the synthetic process, along with the detailed mechanism of formation of the hierarchical interconnected porous channels and hollow N-C nanocages. The PS component acted as the dispersed phase in the spinning solution of PAN, ZIF-8, V_2O_5, and DMF because of its highly incompatible nature based on the different solubility parameters (PAN: 12.5 (cal $cm^{-3})^{1/2}$, PS: 9.1 (cal $cm^{-3})^{1/2}$).[52] This resulted in the formation of an island-like PS phase, having initially oval-shaped granules that subsequently became stretched under the high electrical field applied during the electrospinning process (Scheme 1-①). The stretching occurs along the fiber length direction in the presence of the V_2O_5/ZIF-8/PAN complex, which is homogeneously distributed. The as-spun fibers were subjected to a single-step carbonitrothermic reduction reaction in the presence of urea as the N source at 800 °C under a N_2 atmosphere (Scheme 1-② and 1-③). This step comprises of two sub-steps depending on the temperature range. During the initial stage (Scheme 1-②), PAN is carbonized, and the dispersed PS phase stretched along the fiber length is decomposed to form numerous longitudinal porous channels. Subsequently, the conversion of V_2O_5 to VN quantum dots occurs through a carbonitrothermic reduction reaction in the presence of urea during the second stage (Scheme 1-③). At the same time, the ZIF-8 polyhedra, which contain zinc as the central metal atom linked to ditopic imidazolate (organic linker) units through N atoms, break down into Zn^{2+}/Zn and organic linkers, which are subsequently converted to N-embedded carbonized products (hollow N-C nanocages), whereas the volatile zinc metal is vaporized at high temperatures (Scheme 1-③). The hollow N-C nanocages eventually entangle with the porous channels to develop a hierarchical, long-range interconnected tunnel-like skeleton. This synergetic and facile mechanism results in a hierarchically porous, highly conductive, multifunctional, and freestanding nanofiber sheet interlayer (Scheme 1-④). The unique N-CNF@VN/HNC nanostructure allows rapid electron conduction through the highly conductive N-C network, and the interconnected tunnel-like porous skeleton ensures enormous pathways for fast lithium-ion transport, as shown in Scheme 1-⑤.

To elucidate the formation mechanism of the unique N-CNF@VN/HNC nanostructure in detail, the characteristics of samples obtained at each step were investigated. The as-spun precursor V_2O_5/ZIF-8/PAN/PS composite fibers obtained after spinning are shown in Fig. 1. In this study, non-aggregated ZIF-8 polyhedra having a rhombic-dodecahedral-type morphology and homogeneous dispersion were prepared before spinning, as shown in Fig. 1a. The average size of the as-synthesized ZIF-8 polyhedra was approximately 50 nm. The XRD pattern of the ZIF-8 polyhedra matches well with those of previous reports (Fig. S1a†).[53–55] Fig. 1b and c show the FE-SEM images of the V_2O_5/ZIF-8/PAN/PS composite fibers obtained after the stabilization of the as-spun nanofibers at 150 °C. The fibers possess a 1-D structure with an average diameter of about 3 μm. The surface of the V_2O_5/ZIF-8/PAN/PS fibers shows a slightly

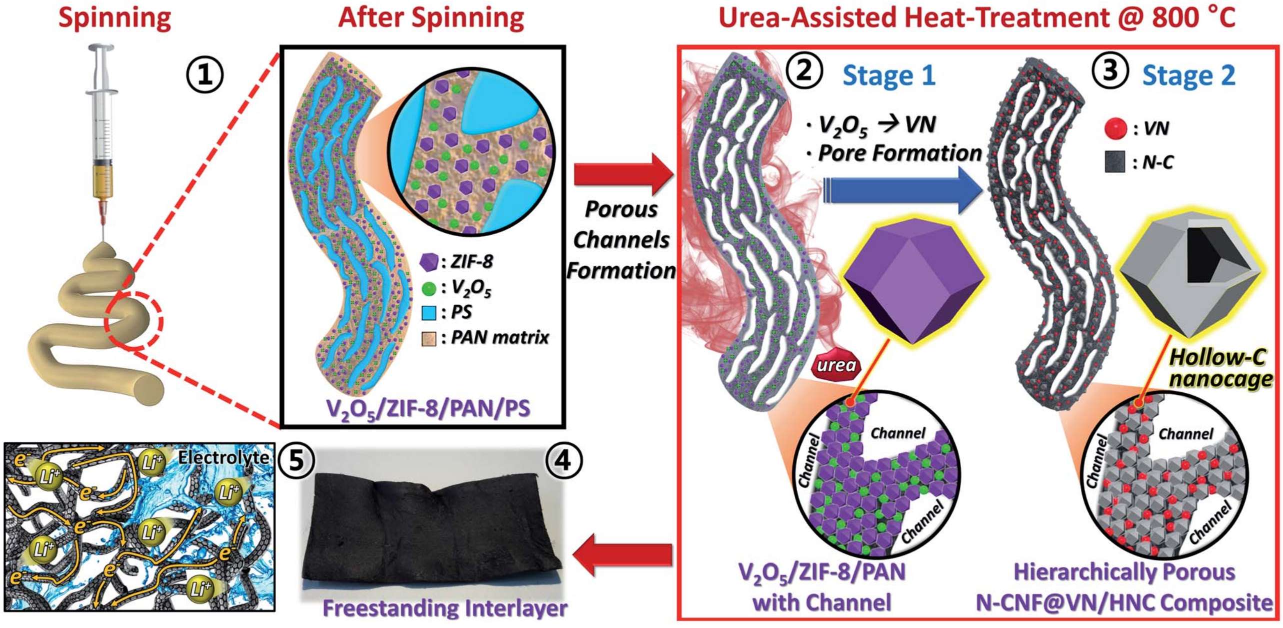

Scheme 1 Formation mechanism of hierarchically porous N-doped C nanofibers comprising VN quantum-dots and hollow N-doped C nanocages (N-CNF@VN/HNC) as a freestanding interlayer for Li–S batteries.

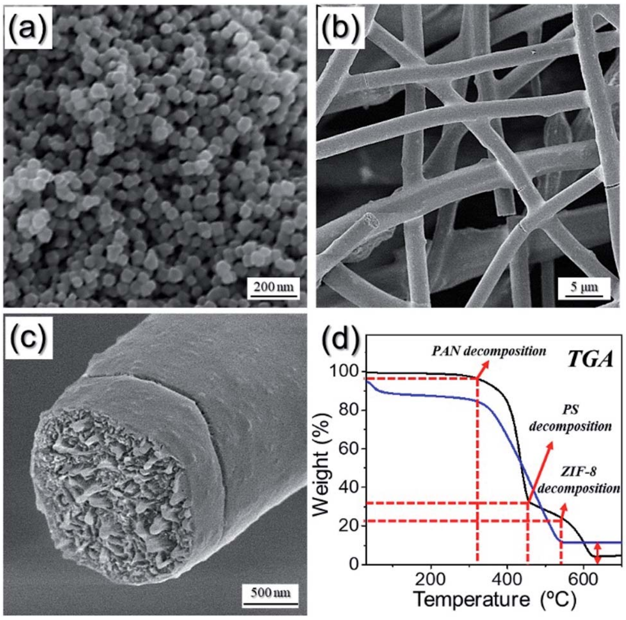

Fig. 1 (a) FE-SEM image of as-synthesized ZIF-8 polyhedra, (b) FE-SEM image, (c) cross-sectional FE-SEM image, and (d) TG curve of as-spun V_2O_5/ZIF-8/PAN/PS composite fibers obtained after stabilization at 150 °C (black line) and as-prepared composite nanofibers after heat-treatment at 800 °C (blue line) in an air atmosphere to quantify the VN quantum dot content.

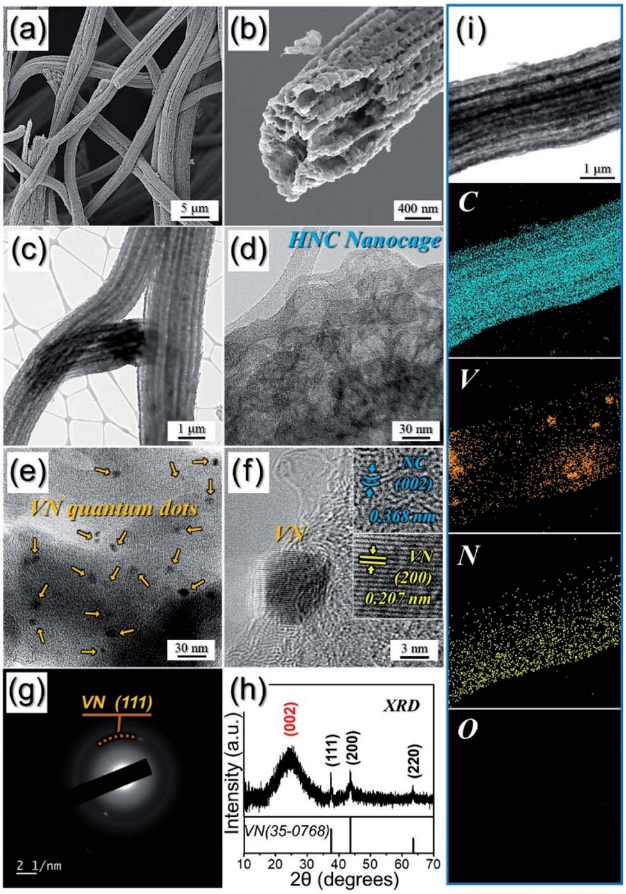

Fig. 2 Morphologies, SAED and XRD patterns, and elemental mapping images of N-CNF@VN/HNC nanofibers obtained after heat-treatment of as-spun V_2O_5/ZIF-8/PAN/PS composite fibers at 800 °C: (a, b) FE-SEM images, (c, d) TEM images, (e, f) HR-TEM images, (g) SAED pattern, (h) XRD pattern, and (i) elemental mapping images.

roughened bumpy surface because of the ZIF-8 polyhedra and V_2O_5 particles (Fig. S2†), which were well dispersed in the structure (Fig. 1b). Additionally, the stretched PS phase was clearly observed on the fractured fiber surface, as shown in Fig. 1c. The TG curve of the V_2O_5/ZIF-8/PAN/PS composite fibers in Fig. 1d (black line) shows multistep weight loss. The first weight loss at around 300 °C is attributed to the carbonization of PAN and PS decomposition, and this was confirmed by TG experiments on PAN and PS separately (Fig. S3†). The second stage of weight loss at around 450 °C is a result of the continuous decomposition of PAN, which is converted to a carbonaceous material. The final stage of weight loss at around 550 °C is attributed to ZIF-8 disintegration.[56] Based on the TG results, the optimal heat-treatment temperature to prepare porous N-C nanofibers embedded with VN-quantum-dot-containing hollow N-C nanocages was chosen as 800 °C. Furthermore, the VN quantum dot content in the as-prepared composite nanofibers after heat-treatment at 800 °C was calculated to be approximately 8.5 wt% by TG analysis in an air atmosphere, as shown in Fig. 1d (blue line).

The hierarchically porous N-C nanofibers comprising VN quantum dots and hollow N-C nanocages (denoted as N-CNF@VN/HNC) as freestanding interlayers were obtained after facile heat treatment of the as-spun V_2O_5/ZIF-8/PAN/PS composite fibers at 800 °C with urea under a N_2 atmosphere, as shown in Fig. 2. The N-CNF@VN/HNC composite nanofibers retained their 1-D structure, having an average diameter of 2.5 μm even after heat treatment at 800 °C. Interestingly, N-CNF@VN/HNC showed continuous long-range tunnel-like porous channels along the fiber length, as shown in Fig. 2b and c. The channels are generated by the decomposition of the elongated PS dispersed phase into gas products, which are phase-segregated from the V_2O_5/ZIF-8/PAN complex during spinning. Along with porous channels, numerous hollow structured N-C nanocages uniformly distributed in the composite can also be clearly seen throughout the nanofiber structure, as shown in Fig. 2d. These hollow N-C nanocages were generated by the removal of highly volatile Zn metal from the ZIF-8 polyhedra in the structure at 800 °C. Specifically, the ZIF-8 polyhedra disintegrate into organic linkers, which are subsequently converted to N-C products, whereas the volatilization of reduced Zn^{2+}/Zn results in the formation of numerous interconnected hollow N-C nanocages.[53,54,57] The well-dispersed hollow N-C nanocages formed a hierarchically unique nanostructure in combination with tunnel-like porous channels. A homogeneous distribution of VN quantum dots of 5 nm in diameter was also observed, as indicated by the arrows in Fig. 2e, and these are well embedded inside the N-C matrix. The clear lattice fringes of 0.207 nm shown in the inset of Fig. 2f are ascribed to the (200) crystal plane of the VN crystal phase. Additionally, clear lattice fringes separated by 0.368 nm can be seen in Fig. 2f, and these correspond to the (002) crystal planes of the N-C phase. The selected area electron diffraction (SAED) and XRD patterns shown in Fig. 2g and h further confirm the presence of N-C (indicated by the (002) peak) and the conversion of the V_2O_5 precursor to VN quantum dots *via* a carbonitrothermic reduction reaction in the presence of urea in N_2 during the heat-treatment process. By applying the Scherrer equation to the characteristic (200) reflection of VN in the XRD pattern, the mean crystallite size of the VN quantum dots was calculated to be 5 nm, which is in good agreement with the VN crystal size observed by high-resolution TEM (Fig. 2f). As shown in the elemental mapping images in Fig. 2i, both VN quantum dots and hollow-structured N-C nanocages were distributed homogeneously in the hierarchically porous N-C nanofiber structure.

The chemical environment and valence state of all the elements in N-CNF@VN/HNC are shown in Fig. 3. The XPS survey spectrum (Fig. 3a) clearly shows V 2p and N 1s signals, along with the characteristic C 1s peak. The deconvolution of the V 2p signal into V $2p_{3/2}$ and V $2p_{1/2}$ is shown in Fig. 3b. The high-resolution V $2p_{1/2}$ spectrum shows a peak at a binding energy around 521.2 eV that belongs to vanadium in the VN structure.[51,58,59] The additional pairs of peaks at 524.1 and 516.2 eV and 522.0 and 515.1 eV are attributed to VO and VNO, respectively, due to the exposure of N-CNF@VN/HNC to an air atmosphere.[50,51,58,60] This suggests the presence of an oxide layer over the VN quantum dots and is in good agreement with the previously reported results.[50,60] Moreover, the existence of a weak V–O peak in the O 1s XPS (Fig. 3c) spectrum also validates the above results.[60] However, it is believed that the content of the oxide layer is so low that it does not affect the Li–S cell performance in this study. Furthermore, the deconvoluted N 1s XPS spectrum shown in Fig. 3d contains two well-resolved peaks at binding energies of 397.6 and 398.8 eV that could be attributed to the N species in the VN quantum dot structure.[58–60] In addition, the peaks at 399.9 and 403.9 eV are assigned to the pyrrolic N and graphitic N species, respectively, produced in the N-doped C framework.[61,62] The C 1s spectrum shown in Fig. 3e contains five peaks at 283.9, 285.3, 286.3, 288.0, and 291.8 eV, corresponding to the doubly coordinated C (C=C), N-doped sp^3 bonded C (N-C/C–C), C–O, C=O, and O–C=O bonds, respectively.[48,59] The presence of N in the C matrix increases the overall electrical conductivity because of its higher electronegativity and smaller atomic radius than that of C.[63] To confirm this hypothesis and to quantify the content of N in the C matrix, elemental analysis (EA) was carried out (Table S1†). The N content in N-CNF@VN/HNC was calculated to be 10.2 wt%, thus confirming the N-doping of the C scaffold, and this is consistent with the elemental mapping images (Fig. 2i) and XPS (Fig. 3d) results. Raman spectroscopy was also carried out to confirm the crystallinity of the C materials in N-CNF@VN/HNC (Fig. 3f). The ratio of intensities of the bands at 1342 cm^{-1} (D-band) and 1582 cm^{-1} (G-band), that is, I_D/I_G, reflects the degree of crystallinity and disorder of the C network.[64] The relatively high I_D/I_G of 1.27 indicates the formation of amorphous C derived from PAN and ZIF-8 polyhedra in the composite during heat treatment.[56,65]

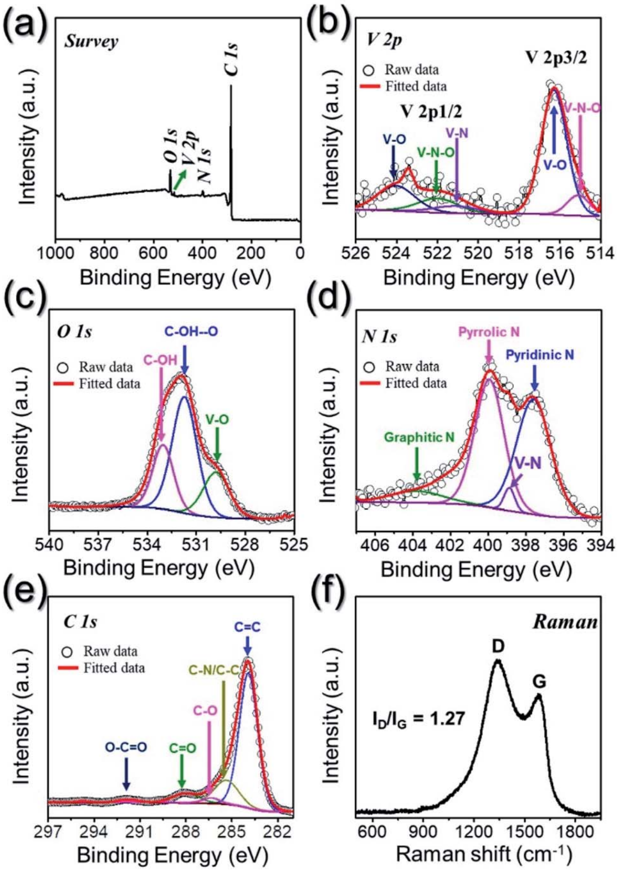

Fig. 3 Characterization of N-CNF@VN/HNC nanofibers: (a) XPS survey spectrum, (b) V 2p XPS spectrum, (c) O 1s XPS spectrum, (d) N 1s XPS spectrum (e) C 1s XPS spectrum, and (f) Raman spectrum.

To demonstrate the structural merits of the hierarchically porous N-C nanofibers comprising VN quantum dots and hollow N-C nanocages as an interlayer for LSBs, comparison samples (1) without VN quantum dots (denoted as N-CNF@HNC) and (2) without either VN quantum dots or hollow N-C nanocages (denoted as N-CNF) were also prepared. For this, ZIF-8/PAN/PS without V_2O_5 (Fig. S4a and b†) and PAN/PS without V_2O_5 and ZIF-8 polyhedra (Fig. S4c and d†) were composited and spun as fibers, as shown in Fig. S4.† The ZIF-8/PAN/PS composite fibers showed an elongated PS dispersed phase, as shown in the cross-sectional FE-SEM image in Fig. S4b.† Likewise, the FE-SEM micrographs of the PAN/PS composite fibers (Fig. S4c and d†) also show stretched PS granules along the fiber length, as observed in the cross-sectional image. After heat-treatment of the ZIF-8/PAN/PS composite fibers at 800 °C, hierarchically porous N-C nanofibers consisting of hollow N-C nanocages without VN quantum dots (N-CNF@HNC) were obtained, as shown in Fig. S5.† The overall structure of N-CNF@HNC is quite similar to that of N-CNF@VN/HNC containing the VN phase, which was prepared using as-spun V_2O_5/ZIF-8/PAN/PS fibers (Fig. 2a–d), as shown in Fig. S5a–d.† Specifically, long-range tunnel-like channels were also generated along the fiber length as a result of the decomposition of the stretched PS granules, as shown in Figs. S5b and c.† Additionally, the hollow N-C nanocages derived from ZIF-8 polyhedra during heat treatment are shown in Fig. S5d.† The porous channels are surrounded by numerous hollow N-C nanocages that are distributed uniformly in the composite fiber structure. The diffuse ring electron diffraction pattern (Fig. S5e†) indicates that N-CNF@HNC is composed of amorphous C formed by the carbonization of PAN and ZIF-8 polyhedra during the heat treatment. In the XRD pattern (Fig. S5f†), the broad peak around 25°, which is assigned to the (002) plane of C, further confirms the formation of amorphous C. The elemental mapping images in Fig. S5g† show the uniform distribution of both C and N in N-CNF@HNC without the VN phase. The chemical nature of N-CNF@HNC is shown in Fig. S6.† The high-resolution C 1s XPS spectrum (Fig. S6b†) contains several peaks corresponding to sp² C=O (288.6 eV), C–O (286.4 eV), C–N (285.3 eV), and C=C (284.2 eV) bonds. The presence of a peak corresponding to C–N bonds confirms the N doping in the C matrix. The high-resolution N 1s spectrum shown in Fig. S6c† indicates the presence of three types of N species: pyridinic N (397.8 eV), pyrrolic N (400.1 eV), and graphitic N (403.4 eV). The atomic content of the N dopant was 13% in N-CNF@HNC, as obtained by EA (Table S1†). From the Raman spectrum (Fig. S6d†), an I_D/I_G value of 1.31 was obtained, indicating that N-CNF@HNC is composed of amorphous N-C, and this is likely formed by carbonization of both PAN and ZIF-8 polyhedra in the structure during heat treatment.

For better comparison, hierarchically porous N-C nanofibers without VN quantum dots or hollow N-C nanocages (N-CNF) were also prepared after heat-treatment of the PAN/PS composite fibers, as shown in Fig. S7.† The porous C nanofibers with continuous and longitudinal channels inside were confirmed by FE-SEM (Fig. S7a†). The XRD pattern (Fig. S7b†), TG curve (Fig. S7c†), Raman spectra (Fig. S7d†), and EA (Table S1†) results indicate that the N-CNF nanofibers are composed of N-doped amorphous C (N content of 11%) alone. The nitrogen adsorption–desorption isotherms of N-CNF@VN/HNC, N-CNF@HNC, and N-CNF nanofibers are shown in Fig. S8.† The initial volume adsorbed at a relative pressure (P/P_0) of 0 is the highest for N-CNF@HNC nanofibers, indicating that they contain mostly micropores (pores with diameter < 2 nm). At $P/P_0 = 0.4$–0.7, a typical hysteresis curve was observed for N–CNF@HNC, indicating the presence of large mesopores (pores with diameters of 2–50 nm). Likewise, at $P/P_0 = 1$, the volume of N_2 adsorbed for N-CNF@HNC is much higher than that for N-CNF@VN/HNC and N-CNF because of the large macropore volume (pores with diameter > 50 nm) of N-CNF@HNC. Overall, the high N_2 adsorption suggests a high surface area of 276 $m^2\ g^{-1}$ (pore volume: 0.46 $cm^3\ g^{-1}$) for N-CNF@HNC, followed by that of N-CNF@VN/HNC (219 $m^2\ g^{-1}$, pore volume: 0.20 $cm^3\ g^{-1}$). In contrast, N-CNF exhibited the lowest surface area of 10 $m^2\ g^{-1}$ (pore volume: 0.07 $cm^3\ g^{-1}$). The relatively low surface area of N-CNF@VN/HNC compared to N-CNF@HNC is because it contains VN quantum dots in the C matrix, whereas the low surface area of N-CNF is attributed to the absence of micropores and mesopores in the structure. These results suggest that the presence of continuous longitudinal channels and interconnected pores in N-CNF@VN/HNC and N-CNF@HNC results in a high surface area, which could be beneficial for better electrolyte percolation and fast reaction kinetics.

The electrochemical performance of the nanofiber-based multifunctional freestanding interlayers for LSBs was investigated to authenticate the effect of the structure and morphology of N-CNF@VN/HNC. CV curves were recorded at a scan rate of 0.1 mV s^{-1} from 1.5 to 2.8 V for the initial cycles of the samples, and the results are shown in Fig. 4a. The obtained CV curves indicate similar electrochemical processes, as evident from the two cathodic peaks located at approximately 2.25 and 1.95 V and one sharp anodic peak at around 2.53 V. The cathodic peak at 2.25 V is associated with the reduction of elemental sulfur (S_8) to higher-order soluble lithium polysulfides (Li_2S_n; $4 \leq n \leq 8$), whereas the cathodic peak at 1.95 V is related to the further reduction of higher-order polysulfides to lower-order insoluble lithium polysulfides (Li_2S_2/Li_2S). During the reverse scan for oxidation, the lower order polysulfides are first oxidized to intermediate lithium polysulfides and then to elemental sulfur at 2.53 V, thus completing the full redox cycle. Moreover, the polarization potential was observed to be the same in all three samples ($\Delta V = 0.29$ V), indicating an almost identical electrochemical environment. However, both N-CNF@VN/HNC and N-CNF@HNC exhibited sharper reduction peaks than N-CNF, indicating better reaction kinetics for N-CNF@VN/HNC and N-CNF@HNC. The CV curves of the samples for the initial five cycles obtained at 0.1 mV s^{-1} are shown in Fig. S9.† The CV curves of the N-CNF@HNC and N-CNF nanofibers overlap because of the precisely reversible electrochemical process. On

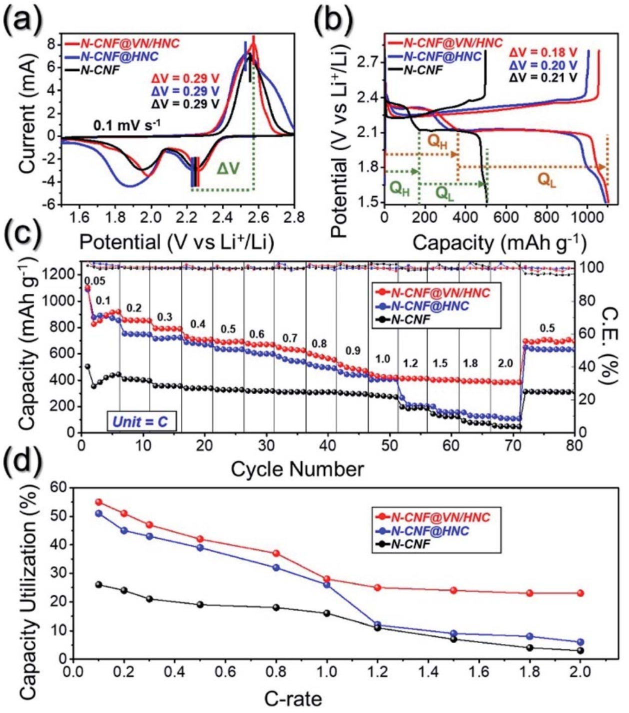

Fig. 4 Electrochemical performances of Li–S cells assembled with different interlayer arrangements: (a) initial CV curves at 0.1 mV s^{-1} (b) initial charge–discharge voltage profiles at 0.05 C-rate. (c) Rate capabilities, and (d) capacity utilization analysis at different C-rates.

the other hand, CV experiments on N-CNF@VN/HNC showed a continuous increase in the current at 1.94 V from the 1st to the 5th cycle because of the activation reaction of N-CNF@VN/HNC. Moreover, the peak currents of N-CNF were minimal during reduction because of the relatively sluggish electrochemical redox reaction of N-CNF inside the Li–S cell. Overall, the shapes of the CV curves for all the synthesized interlayers remained unchanged. However, the slight variation in the peak current suggests a difference in the discharge capacity.

To understand the effect of the as-prepared freestanding interlayers on the electrochemical performance further, Li–S cells were assembled by using N-CNF@VN/HNC, N-CNF@HNC, and N-CNF as interlayers, and subjected to charge–discharge cycles. Fig. 4b shows the initial charge–discharge voltage profiles of all the assembled cells with different interlayer arrangements at 0.05C. The positions of the voltage plateau in the charge–discharge profiles match the peak positions observed in the CV curves exactly. The voltage profile also suggests that the redox reactions only occur between sulfur and lithium polysulfides during the charge–discharge process. All the profiles show two clear voltage regions, starting with a short discharge voltage plateau at 2.30 V that corresponds to the reduction of sulfur to higher-order polysulfides followed by a voltage slope until around at 2.10 V, which is attributed to the formation of middle-order polysulfides. The voltage plateau between 2.35 and 2.10 V is denoted as "Q_H" in the figure. After this point, a longer voltage region of 2.10–1.50 V was observed that corresponds to the full conversion of middle-order polysulfides to the end discharge product, *i.e.*, Li_2S. The voltage region between 2.10 and 1.50 V is denoted as "Q_L" and constitutes most of the discharge capacity of a Li–S cell. In an ideal Li–S cell, where S utilization is 100%, a discharge capacity of 419 mA h g^{-1} corresponds to "Q_H," whereas the remaining 1256 mA h g^{-1} comes from the "Q_L" region.[66] As observed, the Li–S cell with the N-CNF@VN/HNC interlayer exhibited the highest Q_H and Q_L values compared to cells with N-CNF@HNC and N-CNF interlayers. The high Q_H and Q_L values for N-CNF@VN/HNC are attributed to the high trapping of soluble sulfur species and better protection because they are prevented from migrating towards the Li anode. This observation is more apparent when considering the voltage hysteresis during charge–discharge for the three different Li–S cells. Among the three different interlayer arrangements, N-CNF@VN/HNC exhibited the lowest voltage hysteresis ($\Delta V = 0.18$ V), which indicates minimal voltage polarization and, hence, better electrochemical performance. The initial discharge capacities of the Li–S cells assembled with N-CNF@VN/HNC, N-CNF@HNC, and N-CNF interlayers were 1103, 1089, and 504 mA h g^{-1}, respectively, at 0.05C. The high sulfur utilization of the N-CNF@VN/HNC interlayer might be attributed to the excellent ionic and electronic conduction and trapping/reuse of soluble sulfur species that prevents their migration towards the anode, and this resulted in the highest initial discharge capacity of the Li–S cell among the prepared samples.

The rate capabilities of Li–S cells at C-rates increasing stepwise from 0.1C to 2.0C are shown in Fig. 4c. At C-rates below 0.3C, the Li–S cells assembled with N-CNF interlayers exhibited fairly low discharge capacities relative to cells with the other samples. However, the cells using N-CNF@VN/HNC or N-CNF@HNC interlayers showed high discharge capacities. The initial discharge capacities of the cell using N-CNF@VN/HNC were 826, 857, 794, 730, 696, 678, 650, 602, 518, 443, 413, 402, 392, and 384 mA h g^{-1} at C-rates of 0.1, 0.2, 0.3, 0.4, 0.5, 0.6, 0.7, 0.8, 0.9, 1.0, 1.2, 1.5, 1.8, and 2.0, respectively. Additionally, the capacities of the N-CNF@HNC interlayer were 877, 754, 715, 689, 639, 619, 579, 520, 463, 404, 266, 200, 155, and 126 mA h g^{-1}, respectively, at the same C-rates. Notably, the cell using N-CNF@VN/HNC exhibited extremely high discharge capacities even at high C-rates greater than 1.0C. This is because of the synergetic effects induced by the morphological and structural features of N-CNF@VN/HNC. VN quantum dots, which are polar and homogeneously distributed in the N-CNF@VN/HNC N-C matrix, efficiently prevent lithium polysulfide diffusion towards the Li anode. Additionally, the interlayer allows the simultaneous trapping and conversion of lithium polysulfide to sulfur species during repeated cycling. Moreover, the hierarchically porous N-C frameworks containing porous channels and hollow N-C nanocages provide both fast electron transfer owing to their high conductivity and enormous conductive channels for better ionic transport and fast redox reactions. These combined effects facilitate fast ionic/electronic transport in the N-CNF@VN/HNC structure during charge–discharge processes, which results in better sulfur utilization with excellent capacity retention and rate kinetics. The charge–discharge profiles at different C-rates (Fig. S10†) clearly suggest that the redox reactions involve a conversion reaction between sulfur and Li_2S through intermediate polysulfides. All the Li–S cells with different interlayers exhibit well-separated discharge voltage plateaus at approximately 2.30 and 2.0 V, especially at low C-rates. However, at higher C-rates, only the cell containing N-CNF@VN/HNC shows distinguished voltage plateaus even at a high C-rate of 2.0C, as evident from the high discharge capacities. The discharge capacities of the cell with the N-CNF@VN/HNC interlayer was extremely high, especially considering the high sulfur content (80 wt%) and high sulfur loading (approximately 4 mg cm^{-2}) in the electrodes. The high capacity of the N-CNF@VN/HNC interlayer is further supported by the analysis of capacity utilization of the cells at different C-rates, as shown in Fig. 4d. The percentage of sulfur utilization in the Li–S cells was calculated by equating the theoretical capacity of sulfur ($1C = 1675$ mA h g^{-1}) to 100%. The cell with the N-CNF@VN/HNC interlayer utilizes almost 55% of the active material at 0.1 C-rate compared to the 51% and 26% for the cells with N-CNF@HNC and N-CNF, respectively. Even at a high current rate of 2.0C, N-CNF@VN/HNC showed approximately 23% sulfur utilization. In contrast, the cells with N-CNF@HNC and N-CNF showed poor capacity utilization rates, and these decreased sharply with an increase in the current rate (*i.e.*, at 2.0 C-rate, 6% for N-CNF@HNC and 3% for N-CNF), indicating low active material utilization during the charge–discharge process. The results clearly suggest that the introduction of N-CNF@VN/HNC as an interlayer not only increases the integrity of the sulfur electrode but also significantly improves the active material participation in the redox reactions.

The cycle performances of Li–S cells with different interlayer arrangements were also investigated at various C-rates (0.1C, 0.5C, 1.0C, and 1.5C), as shown in Fig. 5. As shown in Fig. 5a, the initial discharge capacities at 0.1C of the cells employing N-CNF@VN/HNC, N-CNF@HNC, and N-CNF interlayers were 875, 820, and 422 mA h g^{-1}, respectively, which correspond to 52%, 49%, and 25% of the theoretical capacity (1C: 1675 mA h g^{-1}). However, after 100 cycles, the discharge capacities of cells with N-CNF@HNC or N-CNF interlayers were 504 and 366 mA h g^{-1}, respectively, which are 61% and 87% of the initial capacities, respectively. In contrast, the cell utilizing the N-CNF@VN/HNC interlayer delivered a discharge capacity of 728 mA h g^{-1} (83% of the initial capacity value) after 100 cycles. Even after 200 cycles, the Li–S cell with the N-CNF@VN/HNC interlayer maintained a discharge capacity of 646 mA h g^{-1} (74% of the initial capacity), having an average capacity decay rate of 0.13% per cycle. Moreover, a high coulombic efficiency of 99.5% after 200 cycles for the Li–S cell with the N-CNF@VN/HNC interlayer suggests better redox kinetics inside the cell. These results clearly indicate that the remarkable cycling superiority of the N-CNF@VN/HNC interlayer can be attributed to the efficient anchoring of lithium polysulfides. In addition, to determine the capacity contribution of N-CNF@VN/HNC to the overall capacity of the cell, the cell employing N-CNF@VN/HNC as an electrode was also assembled under identical conditions and cycled at a current density of 100 mA g^{-1} (Fig. S11†). Interestingly, except for the high initial discharge capacity, the N-CNF@VN/HNC electrode exhibits almost zero capacity over 60 consecutive cycles from 1.5 to 2.8 V. This clearly indicates that N-CNF@VN/HNC only acts as a reservoir to provide various chemisorption sites for polysulfide trapping, ensuring their reuse, as well as numerous conductive channels for fast ion transfer.

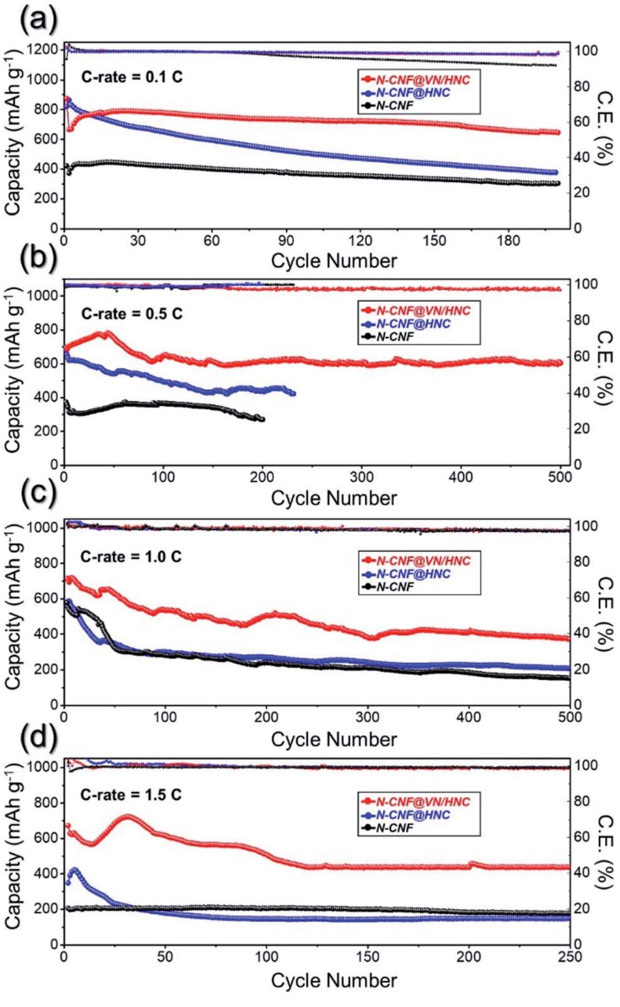

Fig. 5 Cycling performance of the Li–S cells with different interlayers at various C-rates: (a) 0.1C, (b) 0.5C, (c) 1.0C, and (d) 1.5C.

Furthermore, long-term cycling stability tests of the cells with different interlayer arrangements were carried out at high C-rates: 0.5C, 1.0C, and 1.5C (Fig. 5b–d). The initial discharge capacities of the cells with N-CNF@VN/HNC, N-CNF@HNC, and N-CNF interlayers at 0.5C were 694, 676, and 373 mA h g^{-1}, respectively, as shown in Fig. 5b. Subsequently, the capacities were stabilized to 610 (after 500 cycles, 88% retention), 423 (after 230 cycles, 63% retention), and 270 (after 200 cycles, 72% retention) mAh g^{-1}. The average capacity decay rates per cycle were calculated to be 0.02% for N-CNF@VN/HNC, 0.16% for N-CNF@HNC, and 0.14% for N-CNF interlayer cells. Similarly, the cell with the N-CNF@VN/HNC interlayer exhibited an initial discharge capacity of 716 mA h g^{-1} and maintained a stable capacity of 374 mA h g^{-1} at the end of the 500th cycle with an average capacity decay rate of 0.09% per cycle at 1.0C (Fig. 5c). In contrast, the N-CNF@HNC and N-CNF interlayer cells exhibited fast capacity fading over long-term cycling. The initial discharge capacities of the N-CNF@HNC and N-CNF interlayer cells were 529 and 611 mA h g^{-1}, respectively, which reduced to 209 and 153 mA h g^{-1} at the 500th cycle with an average decay rate of 0.12% and 0.15% per cycle, respectively (Fig. 5c). At a high C-rate of 1.5C (Fig. 5d), the initial discharge capacities of the cells with N-CNF@VN/HNC, N-CNF@HNC, and N-CNF interlayers were 673, 348, and 205 mA h g^{-1}, respectively, which stabilized to 437, 149, and 178 mA h g^{-1} at the end of the 250th cycle. Additionally, the extended cycling performance of Li–S cells with the N-CNF@VN/HNC interlayer at 0.1, 0.5 and 1.5 C-rates is shown in Fig. S12,† which clearly validates the structural advantages of the interlayer during long-term cycling. The Li^+-ion storage properties of the Li–S cell using N-CNF@VN/HNC as an interlayer was compared with those of cells using other nanomaterials as cathodes or interlayers reported in previous studies, and the results are summarized in Table S2 and Fig. S13.† The cell using N-CNF@VN/HNC as an interlayer showed the best reported areal capacities at the highest sulfur loading compared with those using other nanomaterials. The superior Li^+ ion storage property of the cell with the N-CNF@VN/HNC interlayer clearly suggests that the diffusion of lithium polysulfide was prevented, resulting in higher active material utilization and hence better rate capability and cycling stability. In addition, efficient polysulfide anchoring through chemical and physical interactions, numerous long-range tunnel-like continuous channels throughout the structure, and the N-doping strategy considerably improves ionic and electronic transfer and redox kinetics, which subsequently results in overall enhanced Li^+ ion storage performance.

The excellent Li^+ ion storage properties of the cell with the N-CNF@VN/HNC interlayer were further verified by EIS measurements of the cell after 100 cycles in the fully charged state, as shown in Fig. 6. The solution resistance (R_s) values of the cells with different interlayers were 2.5–7.7 Ω, suggesting similar electrode–electrolyte interactions. In addition, the cell having the N-CNF@VN/HNC interlayer exhibited the lowest charge transfer resistance (R_{ct}) value (54.3 Ω) compared to the cells having N-CNF@HNC (58.2 Ω) and N-CNF (68.0 Ω) interlayers. This proves that the introduction of the N-CNF@VN/HNC interlayer not only improves the electrode–electrolyte interactions but also increases cathode integrity in terms of active material utilization, which results in improved reaction kinetics inside the Li–S cell. For the R_{ct} values after the 100th cycle (Fig. 6b), all cells showed a decrease, indicating that electrode pulverization did not occur during cycling. However, the cell with the N-CNF@VN/HNC interlayer showed the lowest R_{ct} value (approximately 21.9 Ω) compared to N-CNF@HNC (35.0 Ω) and N-CNF (48.5 Ω), demonstrating the advantage of incorporation of the N– CNF@VN/HNC interlayer in enhancing the electrochemical performances of Li–S cells. The Li-ion diffusion coefficients (D_{Li^+}) of the cells were calculated with respect to the different interlayer arrangements. All cells were cycled from 0.05 to 0.3 mV s^{-1}, and the corresponding CV curves are shown in Fig. 6c–h. In the CV curves, a single anodic peak labeled "A" at around 2.55 V and two clearly reversible cathodic peaks marked as "B" and "C" at 2.25 and 2.0 V, respectively, were observed. The anodic peak at 2.55 V corresponds to the oxidation of lower-order lithium polysulfides (Li_2S_x, $2 \leq x \leq 4$) to higher-order lithium polysulfides (Li_2S_x, $4 \leq x \leq 8$), which were subsequently oxidized further to elemental sulfur (S_8). Similarly, two well-separated cathodic peaks correspond to the reduction of elemental sulfur to higher-order lithium polysulfides (Li_2S_x, $x \geq 4$) at 2.25 V, followed by complete reduction to lower-order lithium polysulfides (Li_2S_x, $1 \leq x \leq 3$). The Randles–Sevcik equation (eqn (1)) was used to calculate the Li-ion diffusion coefficients (D_{Li^+}).[67]

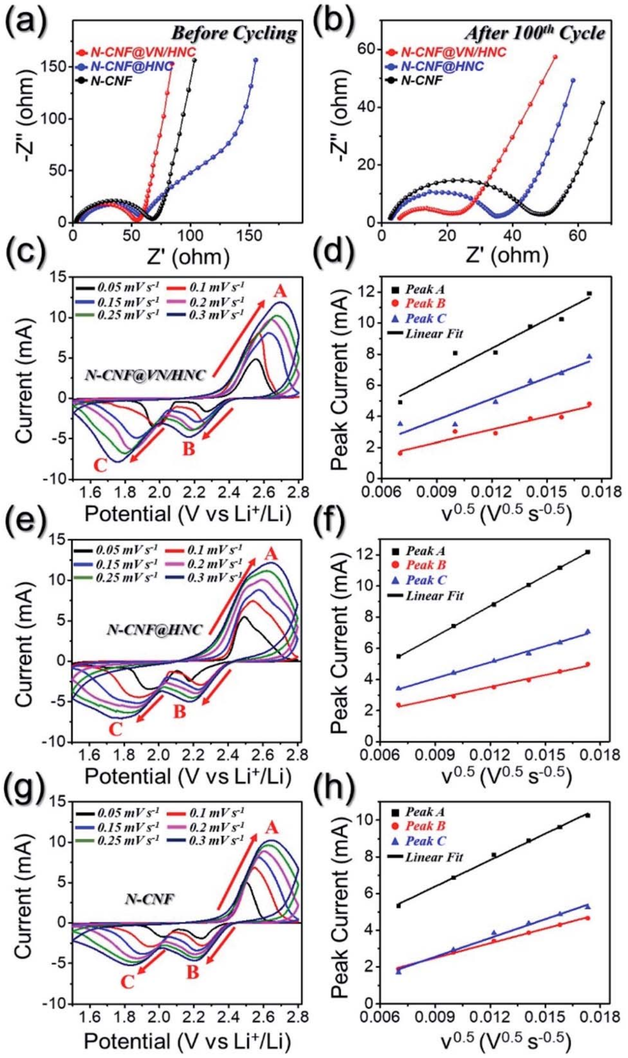

Fig. 6 Nyquist impedance plots, CV curves and their corresponding linear fits to the peak current values of the cells with different interlayers: Nyquist impedance plots (a) before cycling and (b) after the 100th cycle at 0.5 C-rate, and CVs and their corresponding linear fits of the cells with (c, d) N-CNF@VN/HNC, (e, f) N-CNF@HNC, and (g, h) N-CNF interlayers.

$$I_p = 2.69 \times 10^5\, n^{1.5}\, A\, D_{Li^+}{}^{0.5}\, C_{Li}\, v^{0.5} \qquad (1)$$

here, D_{Li^+} is the lithium-ion diffusion coefficient ($cm^2\ s^{-1}$), I_p is the cathodic/anodic peak current (A), n is the number of electrons involved in the reaction ($n = 2$), A is the area of the electrode (cm^2), C_{Li} is the lithium-ion concentration ($moL\ L^{-1}$), and v is the scanning rate ($V\ s^{-1}$). The plots between the anodic/cathodic peak current I_p and the square root of the scan rate ($v^{0.5}$) for different interlayer configurations are shown in Fig. 6d, f, and h and the obtained values are listed in Table S3.† The cell with the N-CNF@VN/HNC interlayer exhibited the highest average diffusion coefficient ($1.60 \times 10^{-7}\ cm^2\ s^{-1}$), which is higher than those of N-CNF@HNC ($1.47 \times 10^{-7}\ cm^2\ s^{-1}$) and N-CNF ($1.01 \times 10^{-7}\ cm^2\ s^{-1}$). The diffusion coefficient results prove that the introduction of N-CNF@VN/HNC as an interlayer effectively prevents the migration of lithium polysulfides from the cathode to the anode side, thus enhancing the redox reaction kinetics. Furthermore, Li–S cells without an interlayer were also assembled and their electrochemical performance was analyzed to reveal the benefits of introducing interlayers. The obtained results are summarized in Fig. S14† along with the relevant discussion.

To understand the interaction between lithium polysulfides and different interlayers, adsorption tests were carried out using a polysulfide solution. For this, sulfur powder and lithium sulfide (1 : 5 mixture) were added to an appropriate amount of DOL : DME (1 : 1, v/v) to form 2.0 M sulfur in the form of Li_2S_6. Three glass vials containing 5.0 mg of N-CNF@VN/HNC, N-CNF@HNC, and N-CNF samples were filled with the lithium polysulfide solution (1.0 mM of Li_2S_6) and stirred inside a glove box. A blank polysulfide solution was also prepared as a standard. As shown in Fig. 7a, the prepared Li_2S_6 solution was initially yellowish, but there was a color change from yellow to colorless after the addition of N-CNF@VN/HNC, N-CNF@HNC, and N-CNF. The color change verifies that all three samples have a strong affinity for lithium polysulfides. To validate the visual results, UV-visible spectroscopy analysis was carried out, and the results are shown in Fig. 7b. The characteristic peak observed at 425 nm in Li_2S_6 solution is attributed to the S_6^{2-} sulfur species[68,69] and disappeared completely after the addition of N-CNF@VN/HNC, N-CNF@HNC, and N-CNF nanofibers because of the strong affinity and effective polysulfide adsorption of the interlayers. Furthermore, the composite nanofiber samples used for polysulfide adsorption tests in Fig. 7a, were recovered, and subsequently dried to remove the solvent. The S 2p XPS signals were analyzed for all the nanofiber samples along with that of commercial sulfur powder as a comparison (Fig. S15†). The commercial sulfur powder exhibits well resolved peaks at binding energies of approximately 162.8 and 164.1 eV that could be assigned to S $2p_{3/2}$ and S $2p_{1/2}$ orbitals, respectively.[70] On the other hand, the polysulfide treated nanofiber samples exhibit weak S $2p_{3/2}$ and S $2p_{1/2}$ signals, suggesting a low amount of free elemental sulfur. Moreover, the presence of two signals centered at 168.4 and 169.5 eV is also evident in as-prepared nanofibers, which indicate the presence of thiosulfate and sulfate species, respectively.[71] The presence of the thiosulfate group indicates the surface redox reaction between lithium polysulfides and VN or N-CNF. It has been reported that the thiosulfate species are helpful in effective anchoring of soluble high-order polysulfides and can convert them to less-soluble lower-order polysulfides thus preventing polysulfide dissolution in the electrolyte.[72] Besides, the similar peak positions for all samples could be due to high nitrogen doping that also facilitates polysulfide anchoring, owing to the high electronegativity of nitrogen. However, the post-cycling morphological results clearly indicate the structural benefits of N-CNF@VN/HNC composite nanofibers for effective polysulfide anchoring, as discussed below.

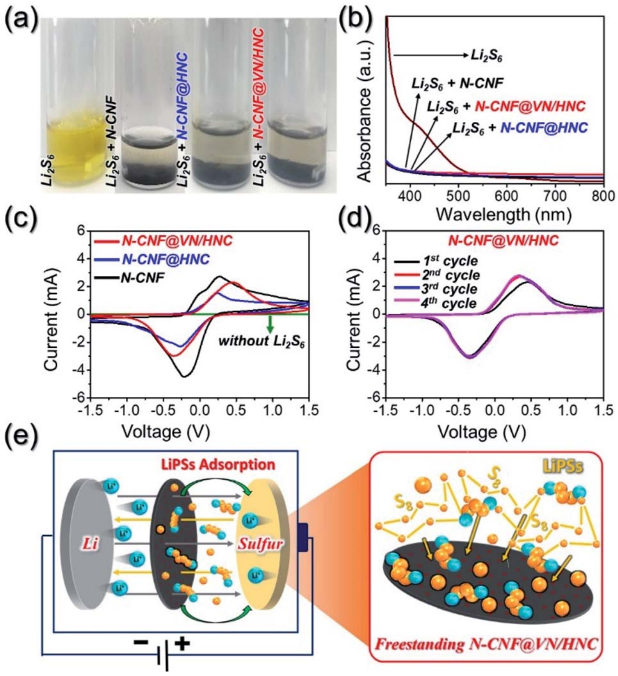

Fig. 7 Adsorption analysis of lithium polysulfides: (a) visual demonstration of polysulfide adsorption using different interlayers, (b) UV-visible spectroscopy of the supernatant solution used in (a), and (c) CV profiles of the first cycle for different symmetric cells at 3 mV s^{-1} from −1.5 to 1.5 V, (d) first four CV cycles for the N-CNF@VN/HNC symmetric cell, and (e) schematic representation of the adsorption mechanism of lithium polysulfide on the N-CNF@VN/HNC interlayer.

To further explore the electrocatalytic activity of N-CNF@VN/HNC composite nanofibers, CV curves were obtained using symmetric cells, in which as-synthesized nanofibers served as the counter and working electrodes with Li_2S_6 in the electrolyte, as shown in Fig. 7c. When cycled from −1.5 to 1.5 V in the presence of Li_2S_6, all interlayer electrodes exhibit similar CV profiles for the initial cycle with slight variation in redox current. However, with further cycles, the CV curve of the N-CNF@VN/HNC symmetric cell almost maintains the original shape (Fig. 7d), whereas those of the N-CNF@HNC and N-CNF symmetric cells (Fig. S16†) display distorted profiles (extra shoulder peaks) compared to the initial curve, implying efficient electrocatalytic activity of N-CNF@VN/HNC towards lithium polysulfide. The structural merits of the N-CNF@VN/HNC interlayer were further verified by analyzing the FE-SEM images after cycling at 1.0 C-rate. Li–S cells featuring different interlayers were carefully opened inside the glove box to remove the interlayer part and subsequently dried at 50 °C to evaporate the electrolyte. Fig. S17† shows the FE-SEM images of the different interlayers facing the sulfur cathode along with the digital photographs of the Celgard separator. The N-CNF@VN/HNC interlayer (Fig. S17a†) shows a continuous smooth fibrous network similar to an uncycled interlayer (Fig. 2a), whereas the N-CNF@HNC interlayer (Fig. S17b†) exhibits slight agglomeration of the discharge products along the fiber length which is more noticeable in the N-CNF interlayer (Fig. S17c†). Besides, the separator color is slightly yellow for the N-CNF@VN/HNC interlayer (Fig. S17d†) compared to those of the other interlayers implying strong immobilization of lithium polysulfides by the VN quantum dots. These results are further supported by the elemental mapping images shown in Fig. S18.† No discharge aggregates were observed for the N-CNF@VN/HNC interlayer, implying that the interlayer not only restricts the diffusion of polysulfide species more efficiently by confining them within the cathode domain but also facilitates their electrocatalytic conversion during the redox reaction (as evident from highest sulfur content). On the other hand, the N-CNF@HNC and N-CNF interlayers exhibited discharge product agglomeration with poor ability to confine sulfur species within the cathode region. These results again confirm the structural supremacy of the N-CNF@VN/HNC interlayer as an efficient reservoir to effectively immobilize lithium polysulfides. Fig. 7c shows the schematic illustration of lithium polysulfides and other sulfur species anchored on the surface of the unique N-CNF@VN/HNC interlayer.

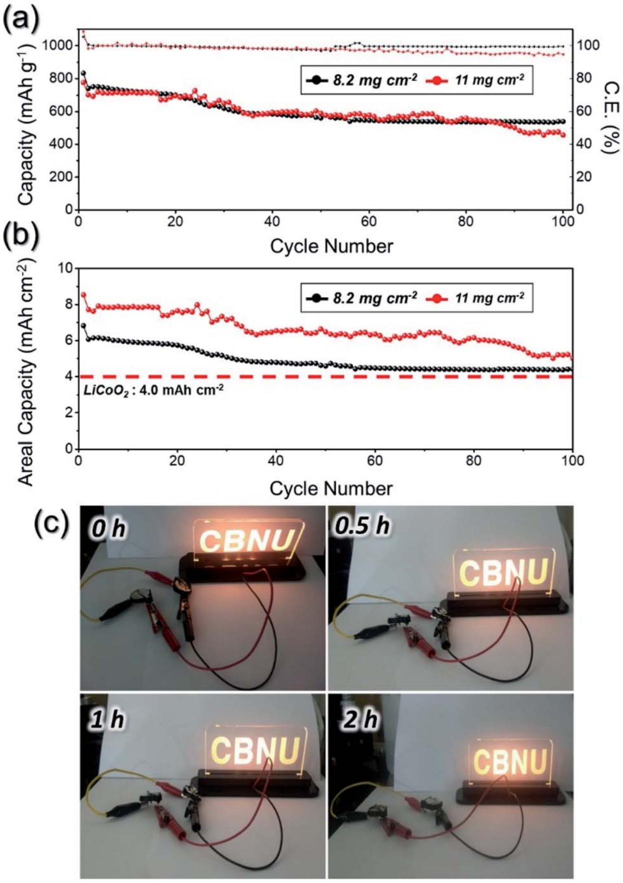

Fig. 8 Cycle performances of Li–S cells employing ultra-high sulfur loading electrodes with N-CNF@VN/HNC (a) at 0.05 C-rate, (b) corresponding cycling performance with areal capacity, and (c) digital photographs of a light-emitting diode (5 V, 10 mW) powered by two cells utilized after rate-capabilities and cycling-performance tests at 0.5C over time.

To obtain better insights into the advantages of N-CNF@VN/HNC as an interlayer, Li–S cells containing electrodes having ultra-high sulfur loadings were cycled for 100 continuous charge/discharge cycles at a C-rate of 0.05, as shown in Fig. 8. The initial discharge capacities of the cells with sulfur loadings of 8.2 and 11.0 mg cm^{-2} were 833 and 776 mA h g^{-1}, respectively (Fig. 8a). Even after 100 cycles, both cells exhibited stable discharge capacities. Furthermore, the cells having sulfur loadings of 8.2 and 11.0 mg cm^{-2} still exhibited 65% and 59% of the initial discharge capacities, respectively, even after 100 charge/discharge cycles. In terms of the areal capacity values (Fig. 8b), the cells also exhibit a high initial areal capacity of 6.8 and 8.5 mA h cm^{-2} for sulfur loadings of 8.2 and 11.0 mg cm^{-2}, respectively, which stabilized to 4.4 and 5.0 mA h cm^{-2}, respectively, after 100 cycles. The areal capacities obtained were much higher than those of the commercially available $LiCoO_2$/graphite system (4.0 mA h cm^{-2}).[73] To validate this further, Li–S cells employing a N-CNF@VN/HNC interlayer after rate capability and cycling performance tests (0.5C) were connected in series and a load was applied across them (Fig. 8c). The series cell combination continuously provided power to the load of a light-emitting diode (5 V, 10 mW) for 2 h, which supports the above findings. Overall, the hierarchically developed free-standing multifunctional N-CNF@VN/HNC interlayer introduced in this study is very promising for the development of advanced metal–sulfur batteries in terms of commercialization, especially because of the use of realistic battery parameters, such as the use of a pure sulfur electrode with a high sulfur content (80 wt% of elemental sulfur), ultra-high sulfur loading (*ca.* 4, 8.2, and 11 mg cm^{-2}), and extremely low electrolyte/sulfur ratio (*ca.* 8 μL mg^{-1}).

Conclusions

In summary, we designed multifunctional, hierarchically porous N-doped C nanofibers comprising VN quantum dots and hollow N-doped C nanocages as functional interlayers for viable Li–S batteries. The interlayer contains well-developed continuous tunnel-like porous channels and hollow N-C nanocages, generated by the decomposition of elongated PS dispersed phase and highly volatile Zn metal from the ZIF-8 polyhedra, respectively. Moreover, the highly conductive N-doped C framework, along with the homogeneously distributed VN quantum dots, provides abundant chemisorption sites for effective lithium polysulfide immobilization. Benefiting from the rational porous and conductive nanostructure design, the interlayer provides numerous conductive pathways for rapid electronic/ionic transfer and therefore, supports fast sulfur redox kinetics reaction. As a result, the assembled Li–S cells with the N-CNF@VN/HNC interlayer and pure sulfur electrodes with a high sulfur content (80 wt%) and high sulfur loadings (*ca.* 4, 8.2, and 11 mg cm^{-2}) show superior rate capabilities and stable cycling performances even at high current rates. We believe that the unique nanostructured interlayer introduced in this study will provide substantial knowledge for the development of viable metal–sulfur batteries based on pure high-loading/-content sulfur electrodes.

Author contributions

Rakesh Saroha designed the idea, performed experiments, and wrote the manuscript. Jang Hyeok Oh conducted data collection and analysis. Young Hoe Seon helped with data analysis tools. Yun Chan Kang, Jae Seob Lee, and Do Won Jeong provided critical feedback. Jung Sang Cho supervised the work along with writing-review and editing. All authors discussed the results and provided valuable suggestions.

Conflicts of interest

There are no conflicts to declare.

Acknowledgements

This work was supported by the National Research Foundation of Korea (NRF) grant funded by the Korean government (MSIP) (Nos. NRF-2021R1A4A200168711, NRF-2017M1A2A2087577, and NRF-2018R1D1A3B07042514).

References

1 Y. C. Jeong, J. H. Kim, S. Nam, C. R. Park and S. J. Yang, *Adv. Funct. Mater.*, 2018, **28**, 1707411.

2 O. H. Kwon, J. H. Oh, B. Gu, M. S. Jo, S. H. Oh, Y. C. Kang, J. K. Kim, S. M. Jeong and J. S. Cho, *Adv. Sci.*, 2020, **7**, 2001358.

3 R. Saroha, T. S. Khan, M. Chandra, R. Shukla, A. K. Panwar, A. Gupta, M. A. Haider, S. Basu and R. S. Dhaka, *ACS Omega*, 2019, **4**, 9878–9888.

4 S. Ghosh, S. M. Jeong and S. R. Polaki, *Korean J. Chem. Eng.*, 2018, **35**, 1389–1408.

5 M. S. Jo, S. Ghosh, S. M. Jeong, Y. C. Kang and J. S. Cho, *Nano-Micro Lett.*, 2019, **11**, 3.

6 L. Fan, P. Sun, L. Yang, Z. Xu and J. Han, *Korean J. Chem. Eng.*, 2020, **37**, 166–175.

7 S. Ghosh, W. D. Yong, E. M. Jin, S. R. Polaki, S. M. Jeong and H. Jun, *Korean J. Chem. Eng.*, 2019, **36**, 312–320.

8 H. S. Kang, P. Santhoshkumar, J. W. Park, G. S. Sim, M. Nanthagopal and C. W. Lee, *Korean J. Chem. Eng.*, 2020, **37**, 1331–1339.

9 Y.-K. Lee, S. Chung, S. Y. Hwang, S. Lee, K. S. Eom, S. B. Hong, G. G. Park, B.-J. Kim, J.-J. Lee and H.-I. Joh, *Korean J. Chem. Eng.*, 2019, **36**, 1543–1547.

10 F. Jin, S. Xiao, L. Lu and Y. Wang, *Nano Lett.*, 2015, **16**, 440–447.

11 Y. Fu, Y. S. Su and A. Manthiram, *Angew. Chem., Int. Ed.*, 2013, **125**, 7068–7073.

12 L. Sun, D. Wang, Y. Luo, K. Wang, W. Kong, Y. Wu, L. Zhang, K. Jiang, Q. Li and Y. Zhang, *ACS Nano*, 2015, **10**, 1300–1308.

13 R. Saroha, J. H. Ahn and J. S. Cho, *Korean J. Chem. Eng.*, 2021, **38**, 461–474.

14 X. Ji, K. T. Lee and L. F. Nazar, *Nat. Mater.*, 2009, **8**, 500.

15 R. Fang, G. Li, S. Zhao, L. Yin, K. Du, P. Hou, S. Wang, H.-M. Cheng, C. Liu and F. Li, *Nano Energy*, 2017, **42**, 205–214.

16 K. Xie, Y. You, K. Yuan, W. Lu, K. Zhang, F. Xu, M. Ye, S. Ke, C. Shen and X. Zeng, *Adv. Mater.*, 2017, **29**, 1604724.

17 Z.-L. Xu, J.-K. Kim and K. Kang, *Nano Today*, 2018, **19**, 84–107.

18 J. Pu, Z. Shen, J. Zheng, W. Wu, C. Zhu, Q. Zhou, H. Zhang and F. Pan, *Nano Energy*, 2017, **37**, 7–14.

19 F. Wu, J. Qian, R. Chen, T. Zhao, R. Xu, Y. Ye, W. Li, L. Li, J. Lu and K. Amine, *Nano Energy*, 2015, **12**, 742–749.

20 S. Moon, Y. H. Jung, W. K. Jung, D. S. Jung, J. W. Choi and D. K. Kim, *Adv. Mater.*, 2013, **25**, 6547–6553.

21 X. Tao, J. Wang, C. Liu, H. Wang, H. Yao, G. Zheng, Z. W. Seh, Q. Cai, W. Li and G. Zhou, *Nat. Commun.*, 2016, **7**, 11203.

22 Z. Shi, W. Feng, X. Wang, M. Li, C. Song and L. Chen, *J. Alloys Compd.*, 2021, **851**, 156289.

23 Z. Song, X. Lu, X. Li, N. Jiang, Y. Huo, Q. Zheng and D. Lin, *J. Colloid Interface Sci.*, 2020, **575**, 220–230.

24 S. Li, Z. Lin, G. He and J. Huang, *Colloids Surf., A*, 2020, **602**, 125129.

25 X. Chen, S. Hu, Y. Liu, A. Ali, S. Li, X. Zhang, X. Li and P. K. Shen, *J. Alloys Compd.*, 2020, **834**, 155096.

26 J. Yao, M. Zhang, G. Han, X. Wang, Z. Wang and J. Wang, *Ceram. Int.*, 2020, **15**, 24155–24161.

27 Y. You, M. Wei, L. Yang, J. Wang, Y. Zhang and J. Xu, *Appl. Surf. Sci.*, 2020, **527**, 146785.

28 Z.-Y. Wang, D.-D. Han, S. Liu, G.-R. Li, T.-Y. Yan and X.-P. Gao, *Electrochim. Acta*, 2020, **337**, 135772.

29 P. Zeng, H. Yu, M. Chen, W. Xiao, Y. Li, H. Liu, J. Luo, J. Peng, D. Shao, Z. Zhou, Z. Luo, Y. Wang, B. Chang and X. Wang, *J. Energy Chem.*, 2020, **51**, 21–29.

30 T. Wu, G. Sun, W. Lu, L. Zhao, A. Mauger, C. M. Julien, L. Sun, H. Xie and J. Liu, *Electrochim. Acta*, 2020, **353**, 136529.

31 Y. Ning, B. Wang, F. Jin, J. Yang, J. Zhang, H. Luo, F. Wu, Z. Zhang, H. Zhang, Y. Zhou and D. Wang, *J. Alloys Compd.*, 2020, **838**, 155504.

32 Z. Yu, J. Zhang, C. Wang, R. Hu, X. Du, B. Tang, H. Qu, H. Wu, X. Liu, X. Zhou, X. Yang and G. Cui, *J. Energy Chem.*, 2020, **51**, 154–160.

33 Y. Wang, G. Wang, P. He, J. Hu, J. Jiang and L.-Z. Fan, *Chem. Eng. J.*, 2020, **393**, 124705.

34 W. Zhang, Y. Zhang, L. Peng, S. Li, X. Wang, S. Cheng and J. Xie, *Nano Energy*, 2020, **76**, 105083.

35 C. Shi, B. Hong, X. Zhang, Q. Xiang, Z. Zhang, K. Zhang, J. Fang and Y. Lai, *J. Electroanal. Chem.*, 2020, **871**, 114312.

36 K. Wu, Y. Hu, Z. Cheng, P. Pan, M. Zhang, L. Jiang, J. Mao, C. Ni, Y. Zhang, Z. Wang, X. Gu and X. Zhang, *J. Alloys Compd.*, 2020, **847**, 156443.

37 H. Ahn, Y. Kim, J. Bae, Y. K. Kim and W. B. Kim, *Chem. Eng. J.*, 2020, **401**, 126042.

38 M. S. Garapati and R. Sundara, *Electrochim. Acta*, 2020, **362**, 137035.

39 Q. Jin, L. Li, H. Wang, H. Gao, C. Zhu and X. Zhang, *Electrochim. Acta*, 2019, **312**, 149–156.

40 L. Chen, H. Yu, W. Li, M. Dirican, Y. Liu and X. Zhang, *J. Mater. Chem. A*, 2020, **8**, 10709–10735.

41 J.-L. Yang, S.-X. Zhao, Y.-M. Lu, X.-T. Zeng, W. Lv and G.-Z. Cao, *J. Mater. Chem. A*, 2020, **8**, 231–241.

42 M. S. Kim, L. Ma, S. Choudhury, S. S. Moganty, S. Wei and L. A. Archer, *J. Mater. Chem. A*, 2016, **4**, 14709–14719.

43 J. Balach, T. Jaumann, M. Klose, S. Oswald, J. Eckert and L. Giebeler, *Adv. Funct. Mater.*, 2015, **25**, 5285–5291.

44 Y.-S. Su and A. Manthiram, *Nat. Commun.*, 2012, **3**, 1166.

45 Y. Han, P. Qi, S. Li, X. Feng, J. Zhou, H. Li, S. Su, X. Li and B. Wang, *Chem. Commun.*, 2014, **50**, 8057–8060.

46 M. Zhong, D. Yang, C. Xie, Z. Zhang, Z. Zhou and X. H. Bu, *Small*, 2016, **12**, 5564–5571.

47 X. Xu, C. Qi, Z. Hao, H. Wang, J. Jiu, J. Liu, H. Yan and K. Suganuma, *Nano-Micro Lett.*, 2018, **10**, 1.

48 J. S. Lee, M. S. Jo, R. Saroha, D. S. Jung, Y. H. Seon, J. S. Lee, Y. C. Kang, D. W. Kang and J. S. Cho, *Small*, 2020, **16**, 2002213.

49 Z. Sun, J. Zhang, L. Yin, G. Hu, R. Fang, H.-M. Cheng and F. Li, *Nat. Commun.*, 2017, **8**, 1–8.

50 L. Ma, H. Yuan, W. Zhang, G. Zhu, Y. Wang, Y. Hu, P. Zhao, R. Chen, T. Chen and J. Liu, *Nano Lett.*, 2017, **17**, 7839–7846.

51 X. Li, K. Ding, B. Gao, Q. Li, Y. Li, J. Fu, X. Zhang, P. K. Chu and K. Huo, *Nano Energy*, 2017, **40**, 655–662.

52 M. S. Jo, G. D. Park, Y. C. Kang and J. S. Cho, *Nanoscale*, 2018, **10**, 13539–13547.

53 J. B. James and Y. Lin, *J. Phys. Chem. C*, 2016, **120**, 14015–14026.

54 N. Nordin, A. Ismail, A. Mustafa, P. Goh, D. Rana and T. Matsuura, *RSC Adv.*, 2014, **4**, 33292–33300.

55 G. Zheng, S. de Marchi, V. López-Puente, K. Sentosun, L. Polavarapu, I. Pérez-Juste, E. H. Hill, S. Bals, L. M. Liz-Marzán and I. Pastoriza-Santos, *Small*, 2016, **12**, 3935–3943.

56 S.-K. Park, J.-S. Park and Y. C. Kang, *J. Mater. Chem. A*, 2018, **6**, 1028–1036.

57 H. Zhang, D. Liu, Y. Yao, B. Zhang and Y. S. Lin, *J. Membr. Sci.*, 2015, **485**, 103–111.

58 Y. Yang, K. Shen, Y. Liu, Y. Tan, X. Zhao, J. Wu, X. Niu and F. Ran, *Nano-Micro Lett.*, 2017, **9**, 6.

59 Y. Wu and F. Ran, *J. Power Sources*, 2017, **344**, 1–10.

60 H.-h. Liu, H.-l. Zhang, H.-b. Xu, T.-p. Lou, Z.-t. Sui and Y. Zhang, *Ceram. Int.*, 2018, **44**, 1583–1588.

61 Y. Liu, L. Liu, Y. Tan, L. Niu, L. Kong, L. Kang and F. Ran, *Electrochim. Acta*, 2018, **262**, 66–73.

62 M. S. Jo, J. S. Lee, S. Y. Jeong, J. K. Kim, Y. C. Kang, D. W. Kang, S. M. Jeong and J. S. Cho, *Small*, 2020, **16**, 2003391.

63 Y. Cheng, L. Huang, X. Xiao, B. Yao, L. Yuan, T. Li, Z. Hu, B. Wang, J. Wan and J. Zhou, *Nano Energy*, 2015, **15**, 66–74.

64 R. Saroha and A. K. Panwar, *J. Phys. D: Appl. Phys.*, 2017, **50**, 255501.

65 C. Chen, K. Fu, Y. Lu, J. Zhu, L. Xue, Y. Hu and X. Zhang, *RSC Adv.*, 2015, **5**, 30793–30800.

66 S. H. Chung and A. Manthiram, *Adv. Funct. Mater.*, 2014, **24**, 5299–5306.

67 J.-Q. Huang, T.-Z. Zhuang, Q. Zhang, H.-J. Peng, C.-M. Chen and F. Wei, *ACS Nano*, 2015, **9**, 3002–3011.

68 P. Xin, B. Jin, H. Li, X. Lang, C. Yang, W. Gao, Y. Zhu, W. Zhang, S. Dou and Q. Jiang, *ChemElectroChem*, 2017, **4**, 115–121.

69 P. Ji, B. Shang, Q. Peng, X. Hu and J. Wei, *J. Power Sources*, 2018, **400**, 572–579.

70 P. M. Shanthi, P. J. Hanumantha, K. Ramalinga, B. Gattu, M. K. Datta and P. N. Kumta, *J. Electrochem. Soc.*, 2019, **166**, A1827.

71 X. Liang, C. Hart, Q. Pang, A. Garsuch, T. Weiss and L. F. Nazar, *Nat. Commun.*, 2015, **6**, 1–8.

72 A. Kumar, A. Ghosh, A. Roy, M. R. Panda, M. Forsyth, D. R. MacFarlane and S. Mitra, *Energy Storage Mater.*, 2019, **20**, 196–202.

73 J. Song, T. Xu, M. L. Gordin, P. Zhu, D. Lv, Y. B. Jiang, Y. Chen, Y. Duan and D. Wang, *Adv. Funct. Mater.*, 2014, **24**, 1243–1250.